npj | Flexible Electronics

www.nature.com/npjflexelectron

ARTICLE OPEN

Check for updates

Solution process formation of high performance, stable nanostructured transparent metal electrodes via displacement-diffusion-etch process

Yaokang Zhang[1,4], Xuyun Guo[2,4], Jiaming Huang[3,4], Zhiwei Ren[3], Hong Hu[1], Peng Li[1], Xi Lu[1], Zhongwei Wu[1], Ting Xiao[1], Ye Zhu[2], Gang Li[3]✉ and Zijian Zheng[1]✉

Transparent electrodes (TEs) with high chemical stability and excellent flexibility are critical for flexible optoelectronic devices, such as photodetectors, solar cells, and light-emitting diodes. Ultrathin metal electrode (thickness less than 20 nm) has been a promising TE candidate, but the fabrication can only be realized by vacuum-based technologies to date, and require tedious surface engineering of the substrates, which are neither ideal for polymeric based flexible applications nor suitable for roll-to-roll large-scale manufacture. This paper presents high-performance nanostructured transparent metal electrodes formation via displacement–diffusion-etch (DDE) process, which enables the solution-processed sub-20-nm-thick ultrathin gold electrodes (UTAuEs) on a wide variety of hard and soft substrates. UTAuEs fabricated on flexible polyethylene terephthalate (PET) substrates show a high chemical/environmental stability and superior bendability to commercial flexible indium–tin-oxide (ITO) electrodes. Moreover, flexible organic solar cells made with UTAuEs show similar power conversion efficiency but much enhanced flexibility, in comparison to that of ITO-based devices.

npj Flexible Electronics (2022)6:4 ; https://doi.org/10.1038/s41528-022-00134-2

INTRODUCTION

The search for solution-processable flexible transparent electrodes to replace the state-of-the-art yet brittle indium–tin oxide (ITO) electrode has been a key challenge in the development of flexible optoelectronic devices, including solar cells[1–5], light-emitting diodes[6–8], photodetectors[9,10], and electrochromic devices[11–13]. Most solution-processed transparent electrodes reported to date are based on mesh-like structures, which are fabricated either by casting of metal nanowires or patterning of microscale metal meshes[14–18]. The metal offers high electric conductivity while the mesh-like structure provides the optical transparency to achieve a high figure of merit (FoM)[19,20]. However, due to the large roughness and the low filling ratio of metal in the mesh, a conductive surface-planarization layer is necessary to smooth the electrode and to ensure efficient and uniform charge transfer[21–23].

On the other hand, ultrathin metal electrodes made of continuous thin layers (<20 nm) of metal (e.g., Cu, Ag, Au) also show good optical transmittance, high electrical conductivity, and superior mechanical flexibility in comparison to ITO. Most importantly, ultrathin metal electrodes are much smoother than the abovementioned mesh-based electrodes, so that are more compatible with optoelectronic devices.

To date, the deposition of ultrathin metal electrodes can only be realized in high vacuum through processes such as sputtering and evaporation[24,25]. Due to the disparity in surface energy between metal and plastic, direct deposition of ultrathin metal electrodes onto polymeric substrates, on which most flexible devices are fabricated, often results in dewetting of the metal and the formation of discontinuous metal islands on the polymer surface[26,27]. This interface mismatch also leads to not only low electrical conductivity but also poor adhesion of the UTME[28,29]. Even with additional surface treatments with oxide supports[30–32], surfactants[33], and molecular monolayers[34] to improve the wettability of metals, it is still very challenging to fabricate high-quality UTME on flexible substrates nowadays. Those ultrathin metal films are usually sandwiched between oxides or dielectric materials to ensure a high FoM and good stability[30,35–37].

Herein, we report a facile chemical process namely displacement–diffusion–etch (DDE), which enables the solution-based fabrication of high-performance and adhesive nanostructured ultrathin gold electrodes (UTAuEs). The DDE process can fabricate UTAuEs at a mild temperature (<150 °C) suitable for a wide variety of flexible substrates at high throughput. The UTAuE significantly outweighs ITO and silver nanowire (AgNW) mesh on polyethylene terephthalate (PET) substrate in the mechanical flexibility and environmental stability, and is superior to mesh-based metal electrodes in the surface smoothness. In comparison to ITO/PET and AgNW/PET electrodes, DDE process also addresses the surface adhesion challenge. We demonstrate the fabrication of highly efficient and flexible organic solar cells (OSCs)[38,39] using the UTAuEs for both normal and inverted device configurations. Both types showed comparable efficiencies to ITO-based control devices, while exhibiting a significantly higher stability under the bending test.

RESULTS

Fabrication of the UTAuE

The DDE process is schematically illustrated in Fig. 1a. Transmission electron microscopy (TEM), high-angle annular dark-field (HAADF) scanning TEM (STEM), electron energy-loss spectroscopy (EELS), and energy-dispersive X-ray spectroscopy (EDS) were

[1]Laboratory for Advanced Interfacial Materials and Devices, Institute of Textiles and Clothing, the Hong Kong Polytechnic University, Hong Kong, China. [2]Department of Applied Physics, the Hong Kong Polytechnic University, Hong Kong, China. [3]Department of Electronic and Information Engineering, Research Institute for Smart Energy, the Hong Kong Polytechnic University, Hong Kong, China. [4]These authors contributed equally: Yaokang Zhang, Xuyun Guo, Jiaming Huang. ✉email: gang.w.li@polyu.edu.hk; zijian.zheng@polyu.edu.hk

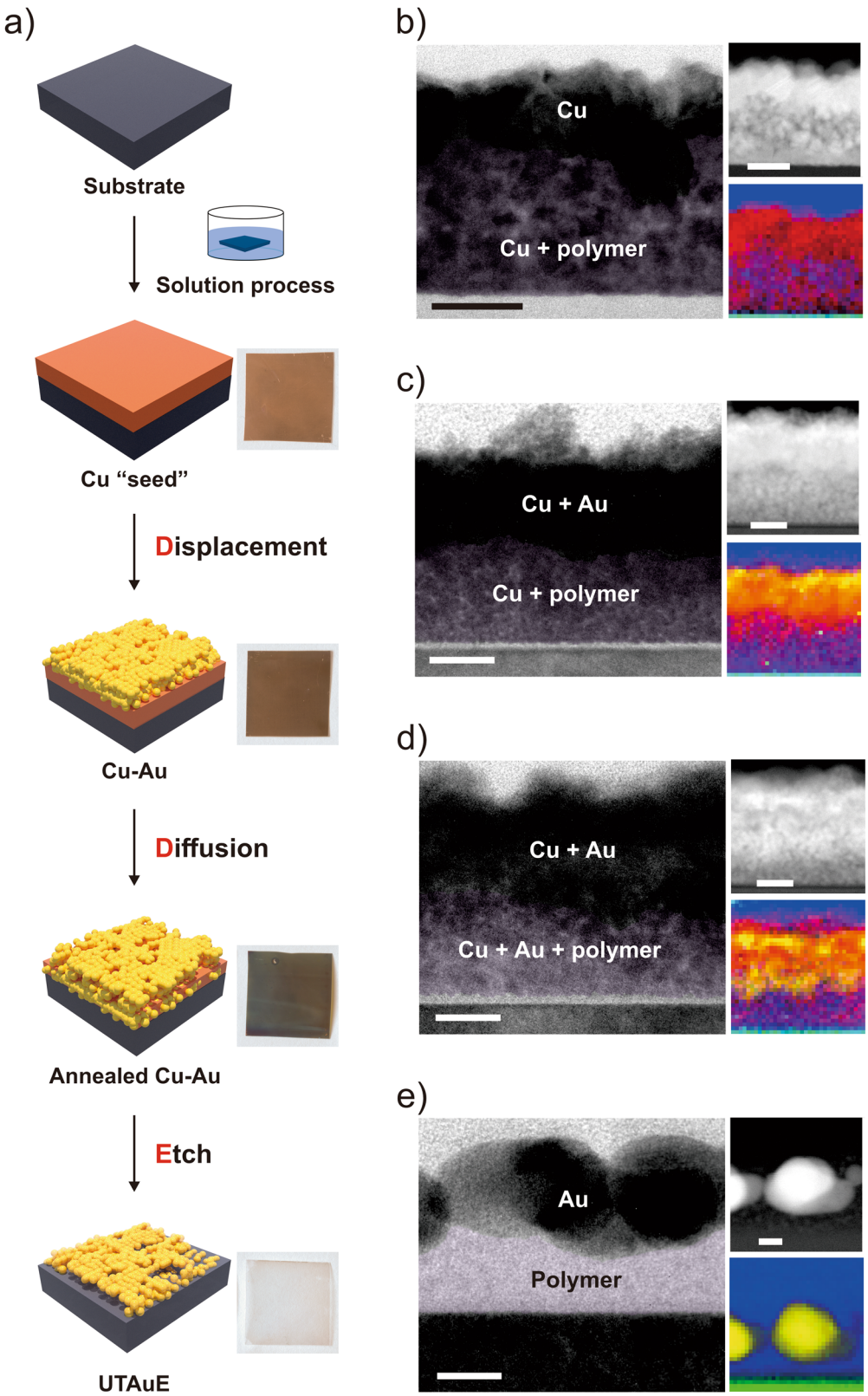

Fig. 1 Fabrication of the UTAuE. a Schematics of the fabrication process of the UTAuE. **b**–**e** Cross-sectional TEM (left), HAADF-STEM (top right), and EELS/EDX mapping (bottom right) images of sacrificial Cu seed, Cu–Au, annealed Cu–Au, and UTAuE, respectively. Green, blue, red, and yellow represent Si, C, Cu, and Au elements on the elemental mapping images, respectively. Scale bars are 50, 20, 20, and 10 nm for **b**–**e**, respectively.

employed to analyze the cross-sectional structure of the fabricated samples. To fabricate the UTAuEs, we first prepared a sacrificing Cu layer on the flexible substrate PET via a solution-based polymer-assisted metal deposition (PAMD) method (see "Methods" for detail)[40]. We studied the influence of Cu layer thickness on the surface morphology of Cu film. Submicron-scale defects can be observed on the surface of 50- and 100-nm-thick samples, which would lead to poor uniformity of Au film after the DDE process. The Cu film became dense and uniform once the thickness was increased to 150 nm. Whereas further increasing the thickness to 200 nm did not change the surface morphology significantly, a thicker Cu layer would require a longer diffusion time for fabricating UTAuEs. Thus, the optimized Cu layer was ~150-nm thick, and was strongly adhered on the PET substrate through a composite-like Cu/polymer interlayer formed during the PAMD process (Fig. 1b and Supplementary Fig. 1). We then partially displaced Cu with Au via a galvanic displacement reaction by immersing the Cu-coated substrate in an aqueous solution of $HAuCl_4$ for 30 s. The Cu layer was gradually displaced by Au from the upper surface and the film thickness of the Cu layer was reduced by ~50% after the displacement (Fig. 1c). We then thermally annealed the sample at 150 °C for 10 min, where Au on the upper surface diffused into the underlying Cu and polymer layer (Fig. 1d and Supplementary Fig. 2)[41,42]. The annealing process also resulted in a larger particle size and higher crystallinity of Au and Cu. Finally, we etched away the Cu by dipping the substrate in $FeCl_3$, leaving an ultrathin layer (less than 20 nm) of multi-grain Au adhered by a thin polymer layer on top of the substrate (Fig. 1e).

XPS analysis

We also studied the chemistry during the DDE process via X-ray photoelectron spectroscopy (XPS). After the galvanic displacement, the majority of Cu element existed in Cu (0) and Cu (I) state, as indicated by the peaks at 932.5 eV and 952.4 eV (Fig. 2a). The detailed spectrum also indicated the existence of a small amount of Cu (II) (Fig. 2d). The following diffusion process caused oxidation of the Cu to Cu (II), resulting in a significant blue shift and satellites at 940–945 eV. Then, the Cu (II) was then removed during the etch process with $FeCl_3$, and the residual Cu remained in a lower valance state (Fig. 2f). The intensity of peaks related to Au 4*f* decreased ~10 times after the diffusion process (Fig. 2b) because the Au element diffused into the Cu layer, leading to a lower concentration of Au on the surface. The detailed spectrum also indicated the majority of Au element was Au (0) for Cu–Au, annealed Cu–Au, and UTAuE (Fig. 2g–i), whereas Au^{3+} was detected after the thermal annealing (Fig. 2h). Meanwhile, we observed C 1*s* peaks relevant to the copolymer on the spectra of the UTAuE sample (Fig. 1c, l) rather than the peaks from C contaminations shown in Fig. 2j, k. This result indicated the UTAuE film is a thin and/or percolative film to allow the escape of photoelectrons.

Scanning electron microscopy (SEM) revealed a percolation morphology of the polycrystalline UTAuE (Fig. 3a) with a random periodicity of 20 nm. The formation of the percolation morphology instead of a dense layer is attributed to the different oxidation states between Au^{3+} and Cu^{2+}; defects occur on the Cu film during the displacement process because the reduction of every two Au^{3+} consumes three Cu atoms[43]. The concentration of the $HAuCl_4$ solution showed a significant impact on the transparency, resistance, and surface roughness of UTAuEs (Supplementary Table 1). In general, when increasing the concentration from 1.25 to 10.0 mM, the optical transmittance of UTAuEs over the entire visible spectrum dropped from ~80 to <30% (Supplementary Fig. 3a), and the average sheet resistance reduced from 595 to 14 $\Omega\,sq^{-1}$ (Supplementary Fig. 3b). The UTAuE/PET fabricated with 2.5 mM $HAuCl_4$ showed >70% transmittance over the entire visible spectrum (Fig. 3b), and sheet resistance of ~45 $\Omega\,sq^{-1}$. The calculated FoMs of the UTAuEs were 0.13, 1.3, 0.076, and $0.00034 \times 10^{-3}\,\Omega^{-1}$ for 1.25, 2.5 5.0, and 10.0 mM $HAuCl_4$, respectively. In comparison, the FoM of ITO/PET was $5.5 \times 10^{-3}\,\Omega^{-1}$.

Optical, electrical, and mechanical properties of the UTAuE

We also found that UTAuEs fabricated with 2.5 mM $HAuCl_4$ showed the lowest surface roughness; the root mean square roughness (r_{rms}) was 11.6 nm (Fig. 3c). The surface roughness increased to 12.4, 14.5, and 106.7 nm at lower (1.25 mM) or higher (5.0 and 10.0 mM) concentrations (Supplementary Fig. 4). Overall, the increase of $HAuCl_4$ concentration resulted in the growth of Au nanoparticle size, as thus increased the roughness of the films. The reaction became very fast when the concentration was increased to 10.0 mM, and the roughness of the film increased dramatically due to the existence of large particles and aggregations. In addition, submicron-scale defects can be observed on the 5 mM and 10 mM samples, which also increased the roughness of the films. Meanwhile, the surface roughness of 1.25 mM sample was slightly higher roughness than that of the 2.5 mM sample because of the poor uniformity of the film at the nanoscale. From the combination of FoM and surface roughness, we determined that the UTAuE prepared with 2.5 mM $HAuCl_4$ was most suitable to be used as transparent electrodes for optoelectronic devices.

The UTAuE possessed remarkable flexibility and environmental stability. The electrical resistance of the UTAuE only increased for less than twofold after 1000 cycles of bending at a very small radius of 1.5 mm. In contrast, the resistance of ITO on PET increased by 10,000-folds after 900 cycles of bending at the same radius due to the brittleness of ITO (Fig. 3d). The electrical resistance of the UTAuE pertained to good stability during the aging test over 2 weeks by placing in an environmental chamber at a high temperature of 120 °C and a relative humidity (RH) of 75%, or immersing in a strong acid (pH < 1) (Fig. 3e). Whereas ITO/PET and AgNW/PET control electrodes also showed a very good thermal stability, these electrodes suffered from a rapid corrosion in acid, especially the ITO electrode which was completely etched away under the same pH condition in just 20 min. In addition, the UTAuE survived the Scotch Tape Peeling Test (Fig. 3f), indicating a very strong binding between the UTAuE and the substrate[44]. The sheet resistance of UTAuE increased slightly from 50 to 53 $\Omega\,sq^{-1}$. In contrast, ITO and AgNW peeled off from the PET substrates after the test due to insufficient adhesion. As a result, a significant increase in sheet resistance was observed. The strong adhesion could origin from the binding between Au and the aromatic groups in the copolymer[45]. Apart from the PET substrate, the DDE process is also adaptable to a wide variety of rigid and flexible substrates including glass, Si wafer, and polydimethylsiloxane, once the sacrificial Cu layer is successfully deposited on those substrates (Supplementary Fig. 5). Whereas $HAuCl_4$ is regarded as an expensive raw material, our method shows a high material utilization and a very low consumption of Au element. To determine the consumption of Au during the displacement process, the change of concentration of $HAuCl_4$ solution was studied with UV–Vis spectrometry. The relationship between $HAuCl_4$ concentration and the absorptance was plotted and fitted in Supplementary Fig. 6, and the concentration of the sample solution was calculated according to Beer–Lambert's Law. According to our calculation, only 0.98 mg Au was consumed during the fabrication process for 12 cm^2 UTAuE, and the utilization efficiency of Au was estimated to be ~47%. The utilization efficiency can be higher for large-scale fabrication, because the Au loss due to the rinsing step can be reduced by recycling the waste rinsing water.

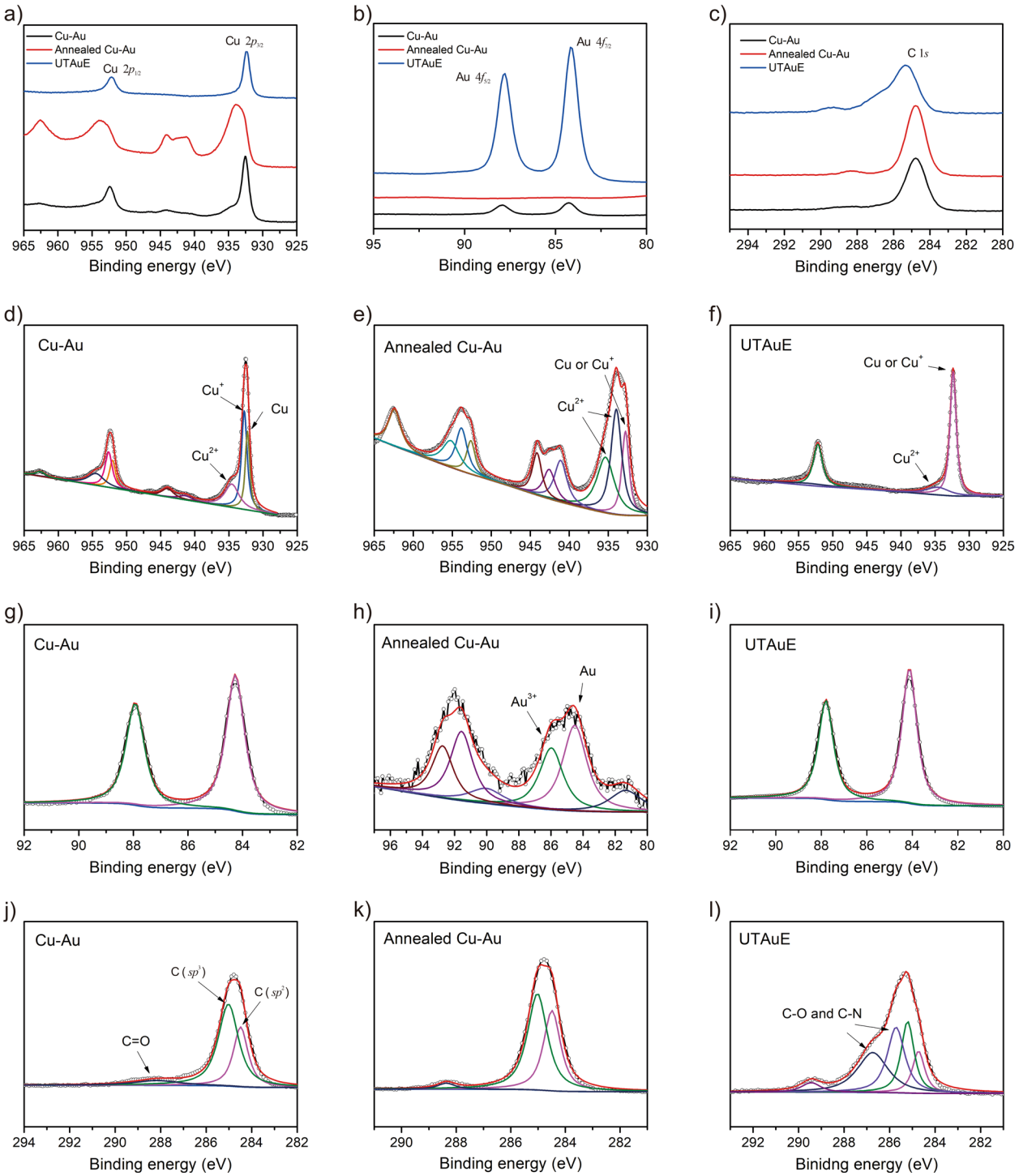

Fig. 2 XPS analysis. a–c XPS Cu 2*p*, Au 4*f*, and C 1*s* spectra of Cu–Au, annealed Cu–Au, and UTAuE. **d–f** Cu 2*p* detail spectra of Cu–Au, annealed Cu–Au, and UTAuE, respectively. **g–i** Au 4*f* detail spectra of Cu–Au, annealed Cu–Au, and UTAuE, respectively. **j–l** C 1*s* detail spectra of Cu–Au, annealed Cu–Au, and UTAuE, respectively.

Performance of OSCs

The smooth topography, high flexibility, and high stabiltiy of UTAuEs are desirable properties of transparent eletrodes of flexible optotelectronic devices. To show the vasatility of the UTAuE, we fabricated flexible OSCs with both normal and inverted configurations (Fig. 4a). The UTAuEs obtained with 2.5 mM $HAuCl_4$ (11.6 nm roughness, 75% transmittance @550 nm, and 45 Ω sq^{-1} average sheet resistance) served as the TEs for the OSCs. The normal and inverted OSCs were constructed with the layouts of PET/UTAuE/PEDOT:PSS/PBDB-T-2F:Y6/PFN-Br/Ag and PET/UTAuE/ZnO/ PBDB-T-2F:Y6/MoO_3/Ag, respectively. The champion normal-structured OSC showed an open-circuit voltage (V_{OC}) of 0.80 V, a short-circuit current density (J_{SC}) of 22.7 mA/cm^2, a fill factor (FF) of 68.1%, and a power conversion efficiency (PCE) of 12.4%. Whereas the inverted OSC showed a slightly lower V_{OC} of 0.79 V, the J_{SC} (23.6 mA cm^{-2}) and FF (70.6%) are higher than those of normal OSC, yielding a PCE of 13.2%. The reference normal and

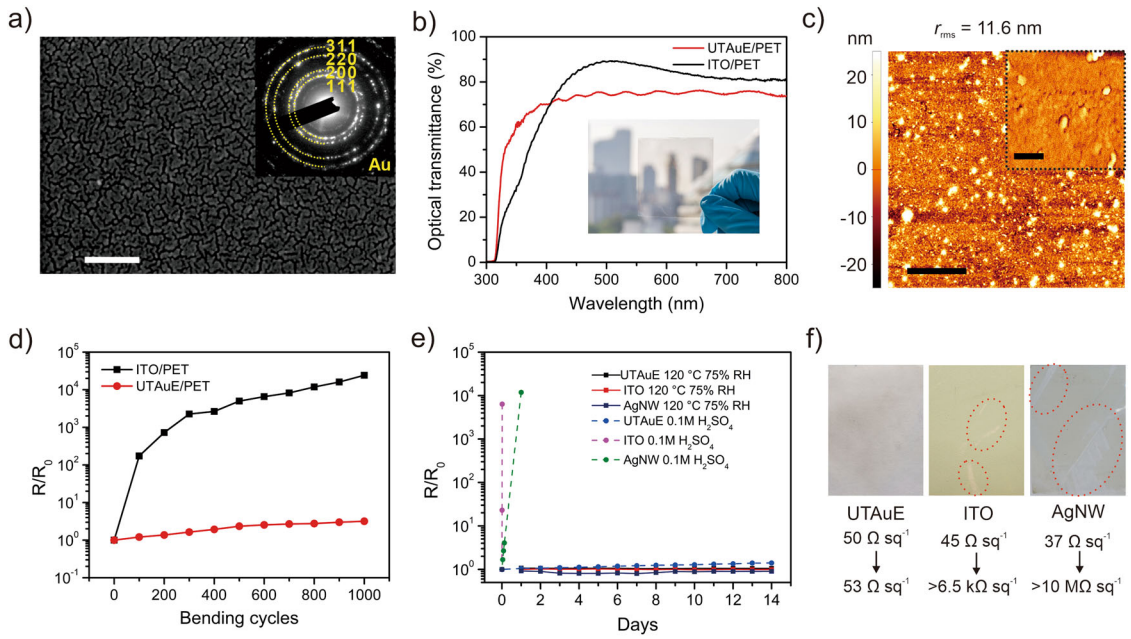

Fig. 3 Optical, electrical, and mechanical properties of the UTAuE. a SEM top view image of the UTAuE. Scale bar is 200 nm. Inset is the TEM diffraction pattern of the UTAuE. **b** UV–Vis transmittance spectra of UTAuE/PET fabricated with 2.5 mM $HAuCl_4$ in comparison to commercial ITO/PET. Inset is a photograph of 5 × 5 cm UTAuE/PET. **c** AFM topographic image of the UTAuE fabricated with 2.5 mM $HAuCl_4$ on PET substrate. Scale bar is 5 μm. Inset is the 1 × 1 μm topographic image of the UTAuE (scale bar is 250 nm). **d** The R/R_0 value of UTAuE/PET and ITO/PET during 1000 cycles of repeated bending at a radius of 1.5 mm. R_0 refers to the initial resistance of each electrode. **e** The R/R_0 of UTAuE/PET, ITO/PET, and AgNW/PET during the 14 days aging test under 120 °C/ 75% RH, or in 0.1 M H_2SO_4. **f** Photographs of UTAuE/PET, ITO/PET, and AgNW/PET after the Scotch Tape Test. Scotch® Flatback Masking Tape 250 (peel adhesion 8.5 N cm^{-1}) is used for this test.

inverted devices fabricated with ITO electrodes showed 12.5% and 13.6% efficiencies, respectively. The current density of the OSCs matched well with the integrated results of the external quantum efficiency (EQE) of the devices (Fig. 4b). The EQE of the UTAuE-based OSCs was higher than that of ITO-based devices at UV and near UV range, which is consistent with the UV–Vis transmission spectra of the electrodes shown in Fig. 3b. In addition, we also fabricated control devices based on vacuum-deposited 20-nm-thick Au electrodes. The devices showed very low J_{SC} due to the low optical transmittance of vacuum-deposited Au films (Supplementary Fig. S7). We tested 40 flexible OSCs with UTAuEs to study the reproducibility (Fig. 4c). The 20 normal devices showed an average efficiency of 10.5%, while ~3/4 of them showed >10% efficiency. Meanwhile, the inverted devices showed higher average efficiency of 11.1%. Finally, the mechanical durability of the flexible solar cells was tested at a bending radius of 1.5 mm for 1000 cycles (Fig. 4d). Less than 5% of PCE drop was observed from the UTAuE-based devices after 1000 cycles of bending. Notably, the inverted OSC only lost <3% of its initial efficiency after the bending test. To the best of our knowledge, this result is one of the best among all reported flexible solar cells at such a small bending radius[46]. In comparison, the PCE of the ITO-based device dropped by >30% after 400 cycling of bending. We compared our devices with the state-of-the-art ITO-free flexible OSCs, our devices showed the highest mechanical durability even if the bending radius is as small as 1.5 mm (Supplementary Table 2).

DISCUSSION

DDE is a versatile chemical process, which enables the solution-based fabrication of nanostructured ultrathin metal electrodes on a wide variety of substrates. In comparison to commercial ITO/PET electrodes, UTAuEs fabricated with the DDE process on PET showed similar FoM, but much improved mechanical flexibility and environmental stability. As a consequence, the UTAuEs were suitable to fabricate highly flexible OSCs without compromising the photovoltaic characteristics. We demonstrated the successful application of the UTAuE as a flexible and transparent electrode for both normal and inverted OSCs, and both UTAuE-based devices showed similar PCEs to those fabricated with ITO electrodes. While the ITO-based OSCs broke down rapidly after several tens of bending, the PCE of the UTAuE-based OSCs pertained over 97% of its initial value after 1000 cycles of bending at a very small bending radius (1.5 mm). The DDE method is a promising low-cost solution-based approach for the large-scale fabrication of transparent electrodes for a wide range of optoelectronic devices.

METHODS

Materials

ITO/PET substrates (R_{sh} = 45 Ω sq^{-1}) were purchased from Zhuhai Kaivo Optoelectronic Technology Co., Ltd.) 4-hydroxybenzophenone (98%), triethylamine (99.5%), methacryloyl chloride (97%), METAC (80 wt.% in water), 2-methoxylethanol (99.8%, anhydrous), polyethylenimine (PEI, 80% in water), 2, 2′-azobis-isobutyronitrile (AIBN, 98%), ammonium tetrachloropalladate [$(NH_4)_2PdCl_4$, 97%], gold chloride ($HAuCl{\cdot}3H_2O$, > 49.0% Au basis) and silver nanowire dispersion were purchased from Sigma-Aldrich. NaOH (>97%), $CuSO_4{\cdot}5H_2O$ (> 98%), potassium sodium tartrate tetrahydrate ($KNaC_4H_4O_6{\cdot}4H_2O$, 99%), Iron (III) chloride ($FeCl_3$, 97%), and formaldehyde (HCHO, 37 wt.% in water) were purchased from Uni-Chem. PM6 (Poly[(2,6-(4,8-bis(5-(2-ethylhexyl-3-fluoro)thiophen-2-yl)-benzo[1,2-b:4,5-b′]dithiophene))-alt-(5,5-(1′,3′-di-2-thienyl-5′,7′-bis(2-ethylhexyl)benzo[1′,2′-c:4′,5′-c′]dithiophene-4,8-dione)]), Y6 (2,2′-((2Z,2′Z)-((12,13-bis(2-ethylhexyl)-3,9-diundecyl-12,13-dihydro-[1,2,5]thiadiazolo[3,4-]thieno[2″,3″:4′,5′]thieno[2′,3′:4,5]pyrrolo[3,2-g]thieno[2′,3′:4,5]thieno[3,2-b]indole-2,10-diyl)bis(methanylylidene)) bis(5,6-difluoro-3-oxo-2,3-dihydro-1H-indene-2,1-diylidene))dimalononitrile), PFN-Br (Poly(9,9-bis(3′-(N,N-dimethyl)-N-ethylammoinium-propyl-2,7-fluorene)-alt-2,7-(9,9-dioctylfluorene)) dibromide) were purchased from Solarmer Materials Inc.

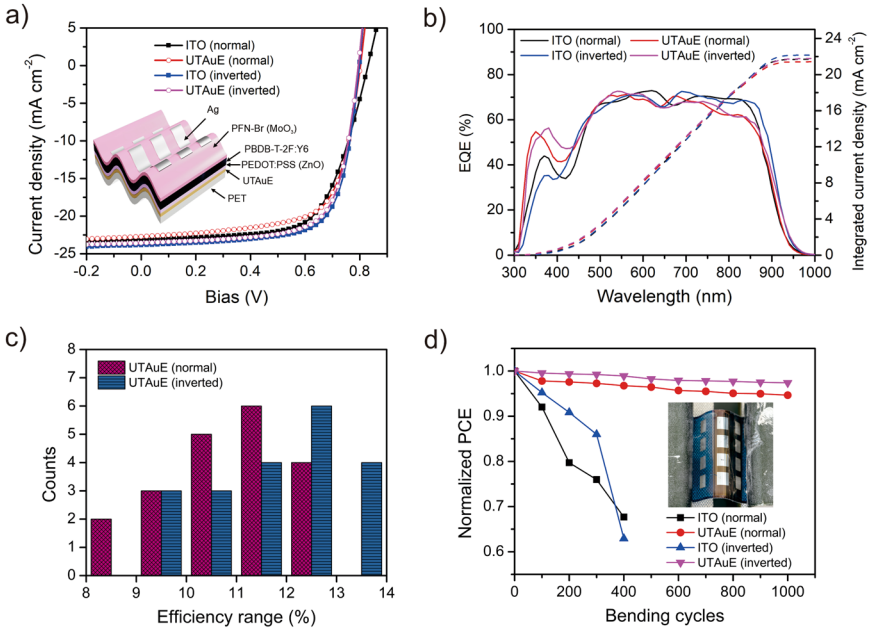

Fig. 4 Performance of OSCs. a J–V curves of the best performing ITO control device and UTAuE-based device. Inset shows the structure of normal and inverted (in bracket) UTAuE-based OSCs. **b** EQE spectra and integrated J_{SC} of the flexible ITO and UTAuE-based OSCs. **c** Statistics of the efficiency range of 40 UTAuE-based OSCs. **d** Bending retention test of ITO control devices and UTAuE-based devices. The bending radius is 1.5 mm.

Synthesis of P(MBP-co-METAC)

The functional copolymer P(MBP-co-METAC) was synthesized via a previously reported method[40]. Briefly, 2 g 4-hydroxybenzophenone and 2 mL triethylamine were dissolved in 100 mL anhydrous CH_2Cl_2, followed by adding of 2 mL methacryloyl chloride in anhydrous CH_2Cl_2 dropwise at 0 °C. After reaction for 24 h, the solution was washed with diluted HCl (10 wt%) and saturated $NaHCO_3$, respectively, three times. Next, the solution was dried by anhydrous Na_2SO_4, and then was evaporated by a rotary evaporator at 60 °C. Finally, the raw product was recrystallized in hexane to obtain the light-yellow needle-like MBP monomer. Next 2 g MBP and 6 g dried METAC (molar ratio 1:5) were added into 2-methoxylethanol (50 mL, Sigma-Aldrich). The solution was bubbled with N_2 gas for 30 min to remove dissolved air. Then, 0.1 g 2, 2′-azobis-isobutyronitrile (AIBN) was added to the solution, and the solution was heated to 65 °C for about 24 h under stirring. After that, the white solid polymer was precipitated with acetone. Finally, purified P(MBP-co-METAC) was obtained by repeated precipitation from ethanol into acetone.

PAMD process

For the samples on PET substrates, 1 wt% P(MBP-co-METAC) copolymer was dissolved in 2-methoxylethanol. The solution was firstly spin-coated onto the target substrates at 3000 rpm for 30 s, followed by thermal annealing at 120 °C for 5 min on a hotplate. The substrates were then cured under a UV lamp for 5 min. Afterward, the substrates were immersed in a 2 wt% solution of $(NH_4)_2PdCl_4$ for 1 min. Finally, the substrates were rinsed with DI water and then immersed in the Cu-plating bath. The recipe of the Cu-plating bath can be found in our previous publication[40].

Fabrication of UTAuEs

The substrates with PAMD Cu were immersed in 2.5 mM $HAuCl_4$ solution for 30 s, and then rinsed with DI water. After drying with compressed air, the substrates were annealed at 150 °C for 10 min on a hotplate. Finally, the substrates were immersed in 1 M $FeCl_3$ solution for 10 s to remove the residual Cu.

Fabrication of OSCs

The UTAuE/PET and ITO/PET substrates were cleaned with DI water, acetone, and isopropanol in an ultrasonication bath for 30 min each by sequence. The substrates were then transferred into a N_2-filled glove box. For normal-structured devices, the PEDOT:PSS (AI 4083) was then spin-coated onto the ITO/PET or UTAuE/PET at 3500 rpm for 40 s, followed by thermal annealing at 100 °C for 10 min. For inverted devices, a solution of ZnO nanoparticles (1:1 in isopropanol) was spin-coated atop the UTAuEs at 2000 rpm for 40 s, and then annealed at 100 °C for 10 min. To prepare the solution of the active layer, 16 mg mL^{-1} PM6 and Y6 (1:1.2) was solved in chloroform with the additive of 0.5% CN and stirred at room temperature overnight. Then the solution was spin-coated at 3000 rpm for 40 s, and annealing at 100 °C for 10 min. For normal-structured devices, PFN-Br (0.5 mg mL^{-1} in methanol) was spin-coated at 3000 rpm for 40 s. For inverted devices, 5 nm MoO_3 was deposited atop the active layer via thermal evaporation. Finally, Ag electrode was deposited by thermal evaporation to complete the whole device.

Characterization

The cross-sectional sample was prepared by a multibeam SEM-FIB system (JEOL, Model JIB-4501), operated under 30 keV Ga^+, equipped with a platinum (Pt) deposition cartridge. To minimize the ion beam damage, the interested area was protected by hundreds of nanometers carbon layer first. After that, a several-micrometer-thick platinum layer was deposited with using the gallium ion beam and then milled to <100-nm-thick lamella gradually. At last, the thin lamella was ex-situ lifted out to the Quantifoil holey carbon Cu grid by glass needle.

Transmission electron microscopy (TEM) and scanning TEM (STEM) were performed using JEOL JEM-2100F TEM/STEM (Tokyo, Japan) operated at 200 kV, equipped Oxford INCA EDS detector and Gatan Enfina electron spectrometer for elemental mapping. Electron energy-loss spectroscopy (EELS) mapping image was carried out with a 13 mrad convergence angle for the optimal probe condition. Energy dispersion of 0.7 eV per channel and 21 mrad collection angle were set up for EELS, HAADF images were acquired with an 89 mrad inner angle simultaneously.

The optical transmittance was measured by Agilent Cary 7000 UV–Vis spectrometer. The AFM topographic images were obtained with an XE-100 AFM (Park Systems, Suwon, South Korea) in non-contact mode. The SEM images were measured by a Carl Zeiss ULTRA 55 scanning electron microscope. The J–V characteristics of the devices were characterized by a Keithley 2400 sourcemeter. To simulate standard sunlight, a solar simulator with AM 1.5 filter (91160, Newport, 450 mW/cm^2) was used as the light source. The solar simulator was calibrated by a standard Si solar cell before use. To determine the active area of the device, a shadow mask (0.04 cm^2) was attached on the device before testing. The EQE of the devices were measured with a standard system consists of a xenon lamp (Oriel 66902,

300 W), a monochrometor (Newport 66902), a Si detector (Oriel 76175_71580) and a dual-channel power meter (Newport 2931_C).

Calculation of FoM

$$\mathrm{FoM} = \frac{T^{10}}{R_S} \quad (1)$$

where T is the optical transmittance at 550 nm and R_s is the sheet resistance[47].

DATA AVAILABILITY

The data that support the findings of this study are available from the corresponding author upon reasonable request.

Received: 16 July 2021; Accepted: 17 December 2021;
Published online: 21 January 2022

REFERENCES

1. Zhang, Y., Ng, S.-W., Lu, X. & Zheng, Z. Solution-processed transparent electrodes for emerging thin-film solar cells. *Chem. Rev.* **120**, 2049–2122 (2020).
2. Fukuda, K., Yu, K. & Someya, T. The future of flexible organic solar cells. *Adv. Energy Mater.* **10**, 2000765 (2020).
3. Hu, X. et al. A mechanically robust conducting polymer network electrode for efficient flexible perovskite solar cells. *Joule* **3**, 2205–2218 (2019).
4. Kaltenbrunner, M. et al. Ultrathin and lightweight organic solar cells with high flexibility. *Nat. Commun.* **3**, 770 (2012).
5. Yan, C. et al. Reducing VOC loss via structure compatible and high lowest unoccupied molecular orbital nonfullerene acceptors for over 17%-efficiency ternary organic photovoltaics. *EcoMat* **2**, e12061 (2020).
6. Han, Y. C., Lim, M. S., Park, J. H. & Choi, K. C. ITO-free flexible organic light-emitting diode using ZnS/Ag/MoO_3 anode incorporating a quasi-perfect Ag thin film. *Org. Electron.* **14**, 3437–3443 (2013).
7. Harkema, S. et al. Large area ITO-free flexible white OLEDs with Orgacon PEDOT: PSS and printed metal shunting lines. *Proc. SPIE* **7415**, 74150T (2009).
8. Gaynor, W. et al. Color in the corners: ITO-free white OLEDs with angular color stability. *Adv. Mater.* **25**, 4006–4013 (2013).
9. Baierl, D., Fabel, B., Lugli, P. & Scarpa, G. Efficient indium-tin-oxide (ITO) free top-absorbing organic photodetector with highly transparent polymer top electrode. *Org. Electron.* **12**, 1669–1673 (2011).
10. Park, S. H. et al. 3D printed polymer photodetectors. *Adv. Mater.* **30**, 1803980 (2018).
11. Baierl, D. et al. A hybrid CMOS-imager with a solution-processable polymer as photoactive layer. *Nat. Commun.* **3**, 1175 (2012).
12. Singh, R., Tharion, J., Murugan, S. & Kumar, A. ITO-free solution-processed flexible electrochromic devices based on PEDOT:PSS as transparent conducting electrode. *ACS Appl. Mater. Interfaces* **9**, 19427–19435 (2017).
13. An, T. et al. Dynamically functioning and highly stretchable epidermal supercapacitor based on vertically aligned gold nanowire skins. *EcoMat* **2**, e12022 (2020).
14. Hu, L., Kim, H. S., Lee, J.-Y., Peumans, P. & Cui, Y. Scalable coating and properties of transparent, flexible, silver nanowire electrodes. *ACS Nano* **4**, 2955–2963 (2010).
15. Wu, H. et al. A transparent electrode based on a metal nanotrough network. *Nat. Nanotechnol.* **8**, 421–425 (2013).
16. Khan, A. et al. High-performance flexible transparent electrode with an embedded metal mesh fabricated by cost-effective solution process. *Small* **12**, 3021–3030 (2016).
17. Lee, J.-Y., Connor, S. T., Cui, Y. & Peumans, P. Solution-processed metal nanowire mesh transparent electrodes. *Nano Lett.* **8**, 689–692 (2008).
18. Deng, B. et al. Roll-to-roll encapsulation of metal nanowires between graphene and plastic substrate for high-performance flexible transparent electrodes. *Nano Lett.* **15**, 4206–4213 (2015).
19. Tang, H. et al. Highly conducting MXene–silver nanowire transparent electrodes for flexible organic solar cells. *ACS Appl. Mater. Interfaces* **11**, 25330–25337 (2019).
20. Chen, X. et al. Printable high-aspect ratio and high-resolution Cu grid flexible transparent conductive film with figure of merit over 80 000. *Adv. Electron Mater.* **5**, 1800991 (2019).
21. Coskun, S., Selen Ates, E., Emrah & Unalan, H. Optimization of silver nanowire networks for polymer light emitting diode electrodes. *Nanotechnology* **24**, 125202 (2013).
22. Han, Y. et al. Efficiency above 12% for 1 cm^2 flexible organic solar cells with Ag/Cu grid transparent conducting electrode. *Adv. Sci.* **6**, 1901490 (2019).
23. Kang, M.-G., Kim, M.-S., Kim, J. & Guo, L. J. Organic solar cells using nanoimprinted transparent metal electrodes. *Adv. Mater.* **20**, 4408–4413 (2008).
24. Gassner, M. et al. Energy consumption and material fluxes in hard coating deposition processes. *Surf. Coat. Technol.* **299**, 49–55 (2016).
25. Baptista, A., Silva, F., Porteiro, J., Míguez, J. & Pinto, G. Sputtering physical vapour deposition (PVD) coatings: a critical review on process improvement and market trend demands. *Coatings* **8**, 402 (2018).
26. Yun, J. Ultrathin metal films for transparent electrodes of flexible optoelectronic devices. *Adv. Funct. Mater.* **27**, 1606641 (2017).
27. Kazmerski, L. L. & Racine, D. M. Growth, environmental, and electrical properties of ultrathin metal films. *J. Appl. Phys.* **46**, 791–795 (1975).
28. Todeschini, M., Bastos da Silva Fanta, A., Jensen, F., Wagner, J. B. & Han, A. Influence of Ti and Cr adhesion layers on ultrathin Au films. *ACS Appl. Mater. Interfaces* **9**, 37374–37385 (2017).
29. Stec, H. M., Williams, R. J., Jones, T. S. & Hatton, R. A. Ultrathin transparent Au electrodes for organic photovoltaics fabricated using a mixed mono-molecular nucleation layer. *Adv. Funct. Mater.* **21**, 1709–1716 (2011).
30. Ren, Z. et al. Strategies for high performance perovskite/crystalline silicon four-terminal tandem solar cells. *Sol. Energy Mater. Sol. Cells* **179**, 36–44 (2018).
31. Han, G. S. et al. Multi-functional transparent electrode for reliable flexible perovskite solar cells. *J. Power Sources* **435**, 226768 (2019).
32. Hong, K. et al. Optical properties of WO_3/Ag/WO_3 multilayer as transparent cathode in top-emitting organic light emitting diodes. *J. Phys. Chem. C.* **115**, 3453–3459 (2011).
33. Henriquez, R. et al. Effect of a metallic surfactant on the electrical percolation of gold films. *Appl. Surf. Sci.* **489**, 403–408 (2019).
34. Yakubovsky, D. I. et al. Ultrathin and ultrasmooth gold films on monolayer MoS_2. *Adv. Mater. Interfaces* **6**, 1900196 (2019).
35. Ji, C., Liu, D., Zhang, C. & Jay Guo, L. Ultrathin-metal-film-based transparent electrodes with relative transmittance surpassing 100%. *Nat. Commun.* **11**, 3367 (2020).
36. Bi, Y.-G. et al. Ultrathin metal films as the transparent electrode in ITO-free organic optoelectronic devices. *Adv. Opt. Mater.* **7**, 1800778 (2019).
37. Zou, J., Li, C.-Z., Chang, C.-Y., Yip, H.-L. & Jen, A. K.-Y. Interfacial engineering of ultrathin metal film transparent electrode for flexible organic photovoltaic cells. *Adv. Mater.* **26**, 3618–3623 (2014).
38. Li, G. et al. High-efficiency solution processable polymer photovoltaic cells by self-organization of polymer blends. *Nat. Mater.* **4**, 864–868 (2005).
39. Cheng, P., Li, G., Zhan, X. & Yang, Y. Next-generation organic photovoltaics based on non-fullerene acceptors. *Nat. Photon.* **12**, 131–142 (2018).
40. Yu, Y. et al. Photoreactive and metal-platable copolymer inks for high-throughput, room-temperature printing of flexible metal electrodes for thin-film electronics. *Adv. Mater.* **28**, 4926–4934 (2016).
41. Chang, C. A. Outdiffusion of Cu through Au: comparison of (100) and (111) Cu films epitaxially deposited on Si, and effects of annealing ambients. *Appl. Phys. Lett.* **55**, 2754–2756 (1989).
42. Madakson, P. & Liu, J. C. Interdiffusion and resistivity of Cu/Au, Cu/Co, Co/Au, and Cu/Co/Au thin films at 25–550 °C. *J. Appl. Phys.* **68**, 2121–2126 (1990).
43. Chauvin, A. et al. Vapor dealloying of ultra-thin films: a promising concept for the fabrication of highly flexible transparent conductive metal nanomesh electrodes. *npj Flex. Electron* **3**, 5 (2019).
44. Geng, Z. & He, J. An effective method to significantly enhance the robustness and adhesion-to-substrate of high transmittance superamphiphobic silica thin films. *J. Mater. Chem. A* **2**, 16601–16607 (2014).
45. Molina, L. M., López, M. J. & Alonso, J. A. Interaction of aromatic molecules with small gold clusters. *Chem. Phys. Lett.* **684**, 91–96 (2017).
46. Yoon, J. et al. Superflexible, high-efficiency perovskite solar cells utilizing graphene electrodes: towards future foldable power sources. *Energy Environ. Sci.* **10**, 337–345 (2017).
47. Haacke, G. New figure of merit for transparent conductors. *J. Appl. Phys.* **47**, 4086–4089 (1976).

ACKNOWLEDGEMENTS

The authors acknowledge the Research Grant Council of Hong Kong (15304919, 15218517, C5037-18G), the Hong Kong Polytechnic University (ZVRP, 8-8408, 1-CDA5), Shenzhen Science and Technology Innovation Commission (JCYJ20200109105003940), the National Natural Science Foundation of China (51961165102), and Guangdong-Hong Kong-Macao Joint Laboratory for Photonic-Thermal-Electrical Energy Materials and Devices (GDSTC No. 2019B121205001).

AUTHOR CONTRIBUTIONS

Y.Z., X.G., and J.H. contributed equally to this work. The study was conceived by Y.Z., J.H., Y.Z., G.L., and Z.J.Z. Y.Z., H.H., P.L., X.L., Z.W., and T.X. discussed the optical, electrical, and mechanical performance of UTAuEs. X.G. performed the TEM characterization. Y.Z., J.H., and Z.R. fabricated and characterized OSCs. Y.Z., G.L., and Z.J.Z. wrote the manuscript, and all authors contributed to the manuscript. Z.J.Z. and G.L. approve the completed version.

COMPETING INTERESTS

The authors declare no competing interests.

ADDITIONAL INFORMATION

Supplementary information The online version contains supplementary material available at https://doi.org/10.1038/s41528-022-00134-2.

Correspondence and requests for materials should be addressed to Gang Li or Zijian Zheng.